# Afterglow imaging and polarization of misaligned structured GRB jets and cocoons: breaking the degeneracy in GRB 170817A

## Ramandeep Gill[1,2]★ and Jonathan Granot[1,3]★

[1]*Department of Natural Sciences, The Open University of Israel, 1 University Road, PO Box 808, Raanana 4353701, Israel*
[2]*Physics Department, Ben-Gurion University, PO Box 653, Beer-Sheva 84105, Israel*
[3]*Department of Physics, The George Washington University, Washington, DC 20052, USA*

## ABSTRACT

The X-ray to radio afterglow emission of GRB 170817A / GW 170817 so far scales as $F_\nu \propto \nu^{-0.6}t^{0.8}$ with observed frequency and time, consistent with a single power-law segment of the synchrotron spectrum from the external shock going into the ambient medium. This requires the effective isotropic equivalent afterglow shock energy in the visible region to increase as $\sim t^{1.7}$. The two main channels for such an energy increase are (i) *radial*: more energy carried by slower material (in the visible region) gradually catches up with the afterglow shock and energizes it, and (ii) *angular*: more energy in relativistic outflow moving at different angles to our line of sight, whose radiation is initially beamed away from us but its beaming cone gradually reaches our line of sight as it decelerates. One cannot distinguish between these explanations (or combinations of them) using only the X-ray to radio $F_\nu(t)$. Here, we demonstrate that the most promising way to break this degeneracy is through afterglow imaging and polarization, by calculating the predicted evolution of the afterglow image (its size, shape, and flux centroid) and linear polarization $\Pi(t)$ for different angular and/or radial outflow structures that fit $F_\nu(t)$. We consider two angular profiles – a Gaussian and a narrow core with power-law wings in energy per solid angle, as well as a (cocoon motivated) (quasi-) spherical flow with radial velocity profile. For a jet viewed off-axis (and a magnetic field produced in the afterglow shock) $\Pi(t)$ peaks when the jet's core becomes visible, at $\approx 2t_p$ where the light-curve peaks at $t_p$, and the image can be elongated with aspect ratios $\gtrsim 2$. A quasi-spherical flow has an almost circular image and a much lower $\Pi(t)$ (peaking at $\approx t_p$) and flux centroid displacement $\theta_{fc}$ (a spherical flow has $\Pi(t) = \theta_{fc} = 0$ and a perfectly circular image).

**Key words:** gravitational waves – polarization – relativistic processes – gamma-ray burst: general – stars: jets.

## 1 INTRODUCTION

GRB 170817A became the first ever bona fide electromagnetic counterpart (e.g. Abbott et al. 2017b, and references therein) of a gravitational wave event, GW 170817, detected by advanced LIGO/VIRGO observatories that marked the merger of two neutron stars (Abbott et al. 2017a). A vigorous observation campaign that started after this discovery led to the detection of the thermal kilonova emission that dominated the optical and near-infrared energy range at early times, as well as the non-thermal afterglow emission in radio and X-rays (Abbott et al. 2017a,b,c; Alexander et al. 2017; Chornock et al. 2017; Coulter et al. 2017; Covino et al. 2017; Cowperthwaite et al. 2017; Drout et al. 2017; Goldstein et al.

2017; Haggard et al. 2017; Hallinan et al. 2017; Kasliwal et al. 2017; Margutti et al. 2017; Nicholl et al 2017; Pian et al. 2017; Smartt et al. 2017; Soares-Santos et al. 2017; Tanvir et al. 2017; Troja et al. 2017; Valenti et al. 2017; Villar et al. 2017; Lyman et al. 2018; Mooley et al. 2018; Ruan et al. 2018). The broad-band afterglow emission from the short-hard gamma-ray burst GRB 170817A, which has been regularly monitored in radio, optical, and X-rays therefore presented a golden opportunity to improve our understanding of the properties of relativistic outflows in GRBs, and in particular their geometry and how their energy is distributed as a function of angle and proper velocity. The afterglow emission continued to rise in flux until $\gtrsim 115$ d post-merger (e.g. Lyman et al. 2018; Margutti et al. 2018; Mooley et al. 2018; Ruan et al. 2018; Troja et al. 2018), where it might have shown a plateau in the light curve at $\sim 138$ d (D'Avanzo et al. 2018; Resmi et al. 2018) and a peak in the X-ray (Margutti et al. 2018) and radio (Dobie et al. 2018) light curves at

★ E-mail: rsgill.rg@gmail.com (RG); granot@openu.ac.il (JG)

$\sim 150-160$ d. It was the rising flux that seriously challenged the simple model of a narrowly beamed, sharp-edged, ultra-relativistic homogeneous jet.

The leading types of models that have been successful at explaining the rising afterglow flux thus far feature an outflow structure that is predominantly either (i) *radial*: a broad distribution of energy with proper velocity $u = \Gamma\beta$ in the outflow with more energy carried by slower material (in the visible region) that gradually catches up with the afterglow shock and energizes it (with a wide-angle quasi-spherical mildly relativistic flow; e.g. Kasliwal et al. 2017; D'Avanzo et al. 2018; Fraija & Veres 2018; Gottlieb, Nakar, & Piran 2018; Hotokezaka et al. 2018; Mooley et al. 2018; Nakar & Piran 2018; Troja et al. 2018), or (ii) *angular*: a jet with angular structure containing an energetic and initially highly relativistic core and sharply falling lower energy wings along which our line of sight is located (e.g. Lamb & Kobayashi 2018; Lazzati et al. 2017a,b; Troja et al. 2017; D'Avanzo et al. 2018; Margutti et al. 2018; Resmi et al. 2018; Troja et al. 2018). In the latter explanation, the radiation from the energetic parts of the jet near its core is initially beamed away from us, and gradually becomes visible as the jet decelerates by sweeping up the external medium. In order to better distinguish between such types of models, or combinations of them, it is useful to look at where most of the energy resides and when it contributes to the observed emission, i.e. when it decelerates for a radial structure, or when its beaming cone reaches our line of sight for a jet with angular structure. Both scenarios can fit the radio and X-ray observations and yield similar late-time behaviour of the light curves. To break this degeneracy in the two models, other diagnostics must be considered.

In this work, we demonstrate that the most promising way to unveil the properties of the outflow, and the distribution of its energy with angle and/or proper velocity $u$, is through afterglow imaging and polarization. To this end, we consider different physically motivated angular and radial outflow structures that can fit the observed light curves and spectrum, $F_\nu(t)$, and calculate for them the predicted evolution of the afterglow image – size, shape, and flux centroid – and linear polarization. The paper is structured as follows. We start by describing the dynamics and structure of the different outflow profiles that are considered here in Section 2. The lateral dynamics are ignored, and the possible implications are discussed in Section 5. Next, in Section 3, we assume that the underlying afterglow emission mechanism is synchrotron and calculate light curves for off-axis emission for the different models, which we also compare with radio, optical, and X-ray observations. We further assume that the magnetic field in the shocked ejecta is completely tangled in the plane orthogonal to the shock normal and calculate the degree of linear polarization for all the models in Section 4. In Section 5, we show the radio images for the different models and calculate the temporal evolution of important characteristics, such as the flux centroid, mean image size, and its axial ratio. Finally, in Section 6, we discuss the importance and feasibility of the diagnostics that are presented in this work and that hold the potential to break the degeneracy between structured jets and quasi-spherical outflows.

## 2 THE OUTFLOW STRUCTURE AND DYNAMICS

### 2.1 A thin shell with local spherical dynamics

For simplicity, we restrict the treatment in this work to axisymmetric outflows. For clarity, let us define a structured jet or outflow as one in which the energy per unit solid angle $dE/d\Omega \equiv \epsilon(\theta)$ and/or the

Lorentz factor (LF) $\Gamma(\theta, r)$ of the jet vary smoothly with the angle $\theta$ from the jet symmetry axis (e.g. Mészáros, Rees, Wijers 1998). As the jet expands into the external medium, it sweeps up mass $dm(r) = \rho(r)4\pi r^2 dr$, where $\rho(r) = n(r)m_p = Ar^{-k}$ (where $m_p$ is the proton mass) and $n(r)$ are the external mass density and number density, respectively, which are assumed here to have a power-law profile with radius $r$. For short GRBs that explode in the interstellar medium (ISM) of their host galaxy, one expects a uniform density ($k = 0$). For long GRBs the outflow expands into a density profile produced by the stellar wind of their massive star progenitor, for which $k = 2$ may be expected for a steady wind.[1]

A thin shell approximation is used for the layer of shocked external medium that carries most of the energy and dominates the observed emission. The lateral dynamics are ignored in this simple treatment, and instead the dynamics at each angle $\theta$ are assumed to be independent of other angles. The local dynamics at each $\theta$ are assumed to correspond to a spherical flow with the local isotropic equivalent jet energy $E_{k,iso}(\theta) = 4\pi\epsilon(\theta)$. At an early stage the shell is assumed to coast with a bulk LF $\Gamma_0(\theta)$ until the deceleration radius $r_d(\theta)$, where most of its energy is used up to accelerate the shocked external medium to $u \approx u_0(\theta)$ and heat it up to a similar thermal proper velocity, so that $m[r_d(\theta)]u_0^2(\theta)c^2 = E_{k,iso}(\theta)$. Here $m(r) = [4\pi A/(3-k)]r^{3-k}$ is the isotropic equivalent swept-up rest mass up to radius $r$, and $u_0(\theta) = \Gamma_0\beta_0 = [\Gamma_0^2(\theta) - 1]^{1/2}$ is the dimensionless proper velocity, where $u_0 \approx \Gamma_0$ for $\Gamma_0 \gg 1$ and $u_0 \approx \beta_0$ for $\Gamma_0 - 1 \ll 1$. The deceleration radius is given by

$$r_d(\theta) = \left[ \frac{(3-k)E_{k,iso}(\theta)}{4\pi Ac^2 u_0^2(\theta)} \right]^{1/(3-k)}$$
$$\approx 1.3 \times 10^{17} E_{53}^{1/3} u_{0,2}^{-2/3} n_0^{-1/3} \text{cm} \quad (k = 0), \qquad (1)$$

where $Q_x$ is the quantity $Q$ in units of $10^x$ times its cgs units. Beyond this radius, the shell starts to decelerate as it continues to sweep up more mass and its evolution becomes self-similar, such that $u(\theta, r) \propto r^{(k-3)/2}$ both during the relativistic phase (Blandford & McKee 1976), and during the Newtonian Sedov–Taylor phase. Radiative losses are neglected, and an adiabatic evolution is assumed from coasting phase through the relativistic and Newtonian self-similar phases. This can be reasonably described as follows. The original shell of rest mass $m_0$ and initial energy $E_0 = (\Gamma_0 - 1)m_0c^2$ is assumed to remain cold as it decelerates and have a kinetic energy of $(\Gamma - 1)m_0c^2$. The swept-up external medium of rest mass $m(r)$ has similar bulk and thermal proper velocities of $u$, so that its total energy excluding its rest energy is $m(r)c^2u^2 = m(r)c^2(\Gamma^2 - 1)$. Therefore, energy conservation reads $(\Gamma_0 - 1)m_0 = E_0/c^2 = m_0(\Gamma - 1) + m(r)(\Gamma^2 - 1)$. Defining the dimentionless radius $\xi(\theta) \equiv r/r_d(\theta)$ one obtains that $m/m_0 = \xi^{3-k}/(\Gamma_0 + 1)$, and energy conservation reads (Panaitescu & Kumar 2000)

$$\frac{\xi^{3-k}}{\Gamma_0 + 1}(\Gamma^2 - 1) + \Gamma - \Gamma_0 = 0, \qquad (2)$$

---

[1]Or for a wind with a constant wind mass-loss rate to velocity ratio, $\dot{M}_w/v_w$. Other values of $k$ or a non-power-law profile are possible if $\dot{M}_w$ and/or $v_w$ vary in the last stages of the massive star's life (e.g. Garcia-Segura, Langer & Mac Low 1996; Chevalier & Li, 2000; Ramirez-Ruiz et al. 2001; Chevalier, Li & Fransson 2004; Ramirez-Ruiz et al. 2005; van Marle et al. 2006; Kouveliotou et al. 2013).
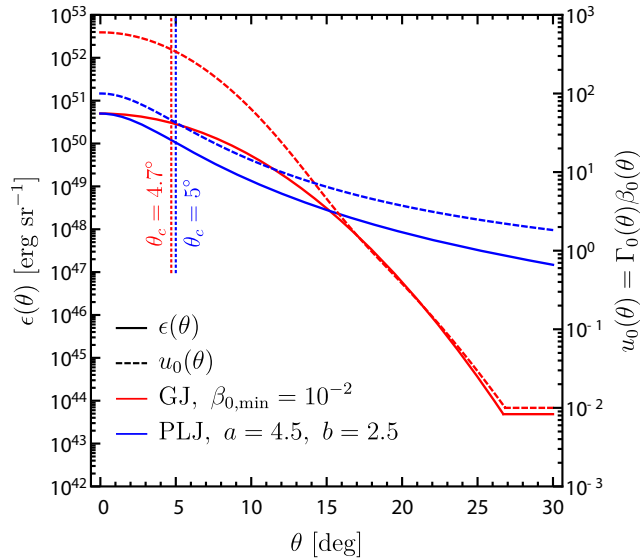
**Figure 1.** Angular profile of the energy per solid angle $\epsilon(\theta) = E_{\rm k,iso}(\theta)/4\pi$ and initial proper velocity $u_0(\theta) = \Gamma_0(\theta)\beta_0(\theta)$ for the two structured jet models considered here – GJ (Gaussian jet) and PLJ (power-law jet). The core angle $\theta_c$ beyond which $\epsilon$ and $u_0$ start to drop sharply is shown with the vertical dotted line.

with the solution

$$\Gamma(\xi) = \frac{\Gamma_0 + 1}{2}\xi^{k-3}\left[\sqrt{1 + \frac{4\Gamma_0}{\Gamma_0 + 1}\xi^{3-k} + \left(\frac{2\xi^{3-k}}{\Gamma_0 + 1}\right)^2} - 1\right]. \quad (3)$$

The expression for $\Gamma(\xi)$ presented above is quite general and applies both when $\Gamma_0$ is ultrarelativistic as well as when $\Gamma_0 \gtrsim 1$. It is similar to the expression presented in equation (4) of Panaitescu & Kumar (2000) in the limit $\Gamma_0 \gg 1$.

### 2.2 Structured jets – with an angular profile

In this work, we consider two distinct angular profiles for the structured jet: (i) A *Gaussian jet* (GJ) for which both $\epsilon(\theta)$ and $\Gamma_0(\theta) - 1$ have a Gaussian profile with a standard deviation or core angle $\theta_c$ (e.g. Zhang & Mészáros 2002; Kumar & Granot 2003; Rossi et al. 2004)

$$\frac{\epsilon(\theta)}{\epsilon_c} = \frac{\Gamma_0(\theta) - 1}{\Gamma_c - 1} = \max\left[\exp\left(-\frac{\theta^2}{2\theta_c^2}\right), \exp\left(-\frac{\theta_*^2}{2\theta_c^2}\right)\right], \quad (4)$$

where $\epsilon_c$ and $\Gamma_c$ are the core energy per unit solid angle and initial core LF, with a floor at $\theta > \theta_*$ corresponding to $\beta_{0,\rm min} = 0.01$, and (ii) a *power-law jet* (PLJ) for which $\epsilon(\theta)$ and $\Gamma_0(\theta) - 1$ decrease as a power law in $\theta$ outside of the core angle, $\theta_c$, such that (e.g. Rossi, Lazzati & Rees 2002; Granot & Kumar 2003; Kumar & Granot 2003; Rossi et al. 2004)

$$\epsilon(\theta) = \epsilon_c\Theta^{-a} \quad, \quad \Theta = \sqrt{1 + \left(\frac{\theta}{\theta_c}\right)^2}, \quad (5)$$

$$\Gamma_0(\theta) = 1 + (\Gamma_c - 1)\Theta^{-b}. \quad (6)$$

Fig. 1 shows the two jet angular profiles for our selected parameters that provide a good fit to the afterglow radio to X-ray light curves.

### 2.3 Outflows with a radial profile, $E_{\rm k,iso}(u)$: (quasi-)spherical shell with energy injection

If the jet cannot break out of the dynamical ejecta of the binary neutron star (BNS) merger and/or the neutrino-driven wind that is launched just after the merger, then it will be chocked. In this case, all of the jet's energy is transferred to a cocoon consisting of shocked jet material and shocked surrounding material, where the latter quickly becomes dominant energetically. The cocoon ultimately breaks out of the surrounding medium that was ejected during the merger and can reach mildly relativistic velocities (typically $\Gamma$ of up to a few or several). The emerging cocoon is expected to form a wide-angle, quasi-spherical flow, and if the external medium's density sharply drops near its outer edge then the cocoon-driven shock would accelerate as it propagates down that density gradient and form an asymptotic distribution of energy with proper velocity $u$ in the resulting outflow that sharply drops with $u$. This is the 'cocoon' scenario (e.g. Kasliwal et al. 2017; Mooley et al. 2018; Nakar & Piran 2018) that has been suggested to explain the initial subluminous gamma-ray and the later broad-band afterglow emission from GRB 170817A.

Alternatively, the BNS merger can give rise to a dynamical ejecta driven by the shock wave that is formed as the two NSs collide that crosses the stars and accelerates down the sharp density gradient in their outer layers, and form an energy distribution that drops less sharply with $u$, $E(> u) \propto u^{-1.1}$ for $u \gg 1$ (e.g. Kyutoku, Ioka, & Shibata 2014).

In both cases most of the energy resides in the slower moving material as compared to a faster moving head of the ejecta. The fastest moving ejecta sweeps up the external medium by driving a relativistic forward afterglow shock into it, and is itself decelerated by a reverse shock, where the two shocked regions are separated by a contact discontinuity (e.g. Sari & Piran 1995). As more external medium is constantly swept up by the forward shock, this double-shock structure gradually decelerates, allowing slower and more energetic ejecta to catch up with it and energize it (e.g. Sari & Mészáros 2000; Nakamura & Shigeyama 2006). This energy injection by the slower and more energetic ejecta results in a slower deceleration of the afterglow shock compared to the case of no energy injection. If $E(> u)$ falls sharply enough with $u$ resulting in a sufficiently fast energy injection rate, this can lead to a gradual rise in the observed flux (see Appendix A1).

The distribution of the ejecta's energy with its initial proper velocity $u_0 = u(t_0)$ can be parametrized as a power law (e.g. Mooley et al. 2018), such that

$$E(> u_0) = E_0\left(\frac{u_0}{u_{0,\rm max}}\right)^{-s} \quad \text{for} \quad u_{0,\rm min} \leq u_0 \leq u_{0,\rm max}. \quad (7)$$

Here, $E_0 = (\Gamma_0 - 1)m_0c^2$ is the energy in the fastest ejecta, of rest mass $m_0$, that is assumed to be cold and initially coasting at $\Gamma_0 = (1 + u_{0,\rm max}^2)^{1/2}$. It is related to the total isotropic equivalent kinetic energy through

$$E_{\rm k,iso} = E_0\left(\frac{u_{0,\rm max}}{u_{0,\rm min}}\right)^s. \quad (8)$$

The observed flux rise suggests a steep distribution with $s \sim 5$–6 (see Appendix A1 or Mooley et al. 2018; Nakar & Piran 2018), which is too steep for the dynamical ejecta scenario mentioned above.

In this scenario of radial gradual energy injection by slower ejecta the deceleration radius is given by

$$r_{\rm d}(\theta) = \left[ \frac{(3-k)E_0(\theta)}{4\pi A c^2 u_{0,\max}^2(\theta)} \right]^{1/(3-k)} \quad (9)$$

$$\approx 1.3 \times 10^{16} E_{0,50}^{1/3} u_{0,\max,2}^{-2/3} n_0^{-1/3} {\rm cm} \quad (k=0, \theta=0) .$$

The dynamical evolution of the emitting region, $u(\xi)$, can be obtained by (numerically) solving the relevant generalization of equation (2) – the dimensionless energy equation

$$\frac{\xi^{3-k}}{\Gamma_0+1} u^2 + \sqrt{1+u^2} - \Gamma_0 \min \left[ \left( \frac{u_{0,\max}}{u} \right)^s , \left( \frac{u_{0,\max}}{u_{0,\min}} \right)^s \right] = 0. \quad (10)$$

We consider two angular profiles for such a wide-angle flow: (i) a uniform spherical shell, for which

$$\epsilon(\theta) = \frac{E_{\rm k,iso}}{4\pi} = \frac{E_0}{4\pi} \left( \frac{u_{0,\max}}{u_{0,\min}} \right)^s , \quad (11)$$

and (ii) a quasi-spherical angular profile that is given by

$$\frac{\epsilon(\theta)}{\epsilon_0} = \frac{u_{0,\min}(\theta)}{u_{\min,0}} = \frac{u_{0,\max}(\theta)}{u_{\max,0}} = \frac{\zeta + \cos^2 \theta}{\zeta + 1} , \quad (12)$$

with $\zeta = 0.1$. The parameter $\zeta$ is chosen to mimic a floor at $u_{0,\{\min,\max\}}(\theta = \pi/2)$. Fig. 2 shows the outflow energy distributions with proper velocity, $E_{\rm k,iso}(>u_0)$ (top panel), and the evolution of $u$ with the observed time $t$ (bottom panel), for these two outflow profiles. The plots are shown for our selected parameters that provide a good fit to the afterglow radio to X-ray light curves.

# 3 CALCULATING THE OBSERVED RADIATION

## 3.1 Synchrotron emission from the forward shock

Synchrotron radiation is usually the dominant emission mechanism throughout the afterglow. Accordingly, we consider synchrotron emission from shock accelerated electrons within the shocked external medium behind the forward shock. For simplicity, we ignore the effects of synchrotron self-absorption and inverse Compton scattering. They are not expected to be very important for our purposes.[2] We do not consider here the emission from the long-lived reverse shock (see e.g. Sari & Mészáros 2000), but in the relevant power-law segment of the synchrotron spectrum its emission is expected to be sub-dominant compared to that of the forward shock for an electron energy distribution power-law index $p > 2$ (where in our case $p \approx 2.2$ is inferred from observations).

The proper internal energy density of the post-shock layer is $e' = (\Gamma - 1)n' m_{\rm p} c^2$, where $n' \approx 4\Gamma n(r)$ is the proper electron number density. A fraction $\epsilon_{\rm e}$ of this energy is shared by the relativistic electrons that have a mean LF of $\langle \gamma_{\rm e} \rangle = \epsilon_{\rm e}(m_{\rm p}/m_{\rm e})(\Gamma - 1)$ and are shock accelerated to form a power-law distribution, such that $n'(\gamma_{\rm e}) \propto \gamma_{\rm e}^{-p}$ for $\gamma_{\rm m} \leq \gamma_{\rm e} \leq \gamma_{\rm M}$, with $\gamma_{\rm m} = [(p-1)/(p-2)]\langle \gamma_{\rm e} \rangle$ for $p > 2$.

[2]Synchrotron-self Compton (SSC) can increase the cooling of the synchrotron emitting relativistic electron, and reduce their cooling break frequency $\nu_{\rm c}$ by a factor of $(1 + Y)^2$ where $Y$ in the Compton parameter. However, we have verified that this effect does not significantly affect our tentative fits to the data, as $\nu_{\rm c}$ still remains (at least marginally) above the measured X-ray energy range.
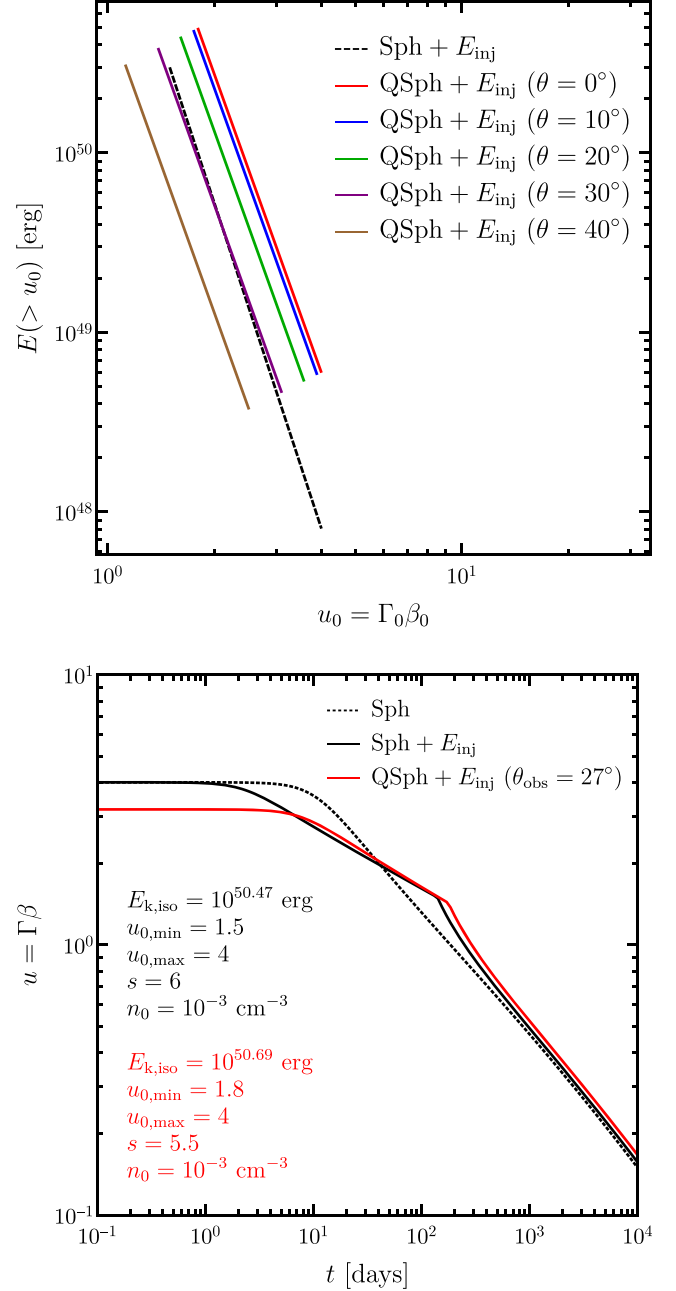




**Figure 2.** (Top) Initial radial velocity stratification for the spherical shell (Sph) and quasi-spherical shell (QSph) models. The relevant parameters are shown in the bottom panel. (Bottom) Dynamical evolution of the Sph model with and without energy injection (due to initial velocity stratification). Also shown is the case of QSph model with energy injection for a viewing angle of $\theta_{\rm obs} = 27°$.

In the rest frame of the emitting plasma, the local comoving sychrotron emissivity (power per unit frequency per unit volume) can be expressed as a broken power law:

$$\frac{P'_{\nu'}}{P'_{\nu',\max}} = \begin{cases} (\nu'/\nu'_{\rm m})^{1/3} & \nu' < \nu'_{\rm m} < \nu'_{\rm c} \\ (\nu'/\nu'_{\rm c})^{1/3} & \nu' < \nu'_{\rm c} < \nu'_{\rm m} \\ (\nu'/\nu'_{\rm m})^{(1-p)/2} & \nu'_{\rm m} < \nu' < \nu'_{\rm c} \\ (\nu'/\nu'_{\rm c})^{-1/2} & \nu'_{\rm c} < \nu' < \nu'_{\rm m} \\ (\nu'/\nu'_{\rm m})^{(1-p)/2}(\nu'/\nu'_{\rm c})^{-1/2} & \nu' > \max(\nu'_{\rm m}, \nu'_{\rm c}) \end{cases} \quad (13)$$

The flux normalization and break frequencies are

$$P'_{\nu',\text{max}} = 0.88 \frac{512\sqrt{2\pi}}{27} \left( \frac{p-1}{3p-1} \right) \frac{q_e^3}{m_e c^2} (\epsilon_B e')^{1/2} n', \qquad (14)$$

$$\nu'_m = \frac{3\sqrt{2\pi}}{8} \left( \frac{p-2}{p-1} \right)^2 \frac{q_e}{m_e^3 c^5} \epsilon_B^{1/2} \epsilon_e^2 (e')^{5/2} (n')^{-2}, \qquad (15)$$

$$\nu'_c = \frac{27\sqrt{2\pi}}{128} \frac{q_e m_e c}{\sigma_T^2} (\epsilon_B e')^{-3/2} \left( \frac{\Gamma}{t_{\text{lab}}} \right)^2, \qquad (16)$$

where $\nu'_m$ and $\nu'_c$ are, respectively, the typical synchrotron frequencies, expressed in the comoving frame, corresponding to electrons moving with Lorentz factors $\gamma_m$ and $\gamma_c$, where the latter are cooling at the dynamical time. Also, in the above equations $q_e$ is the elementary charge and $\sigma_T$ is the Thomson cross-section. The swept-up external rest mass per unit shock area is $m(r)/4\pi r^2 = Ar^{1-k}/(3-k)$, which for a uniform shell implies a comoving radial width of $\Delta' = r/4(3-k)\Gamma$. The shell's isotropic equivalent comoving spectral luminosity $L'_{\nu'}$ (the total power per unit frequency assuming a spherical shell with the local properties at any given angle $\theta$ from the jet axis) is related to $P'_{\nu'}$ through the volume of the emitting region, and is therefore given by $L'_{\nu'}/P'_{\nu'} = L'_{\nu',\text{max}}/P'_{\nu',\text{max}} = V' = 4\pi r^2 \Delta' = \pi r^3/(3-k)\Gamma \propto r^3/\Gamma(r)$.

The synchrotron emissivity given above implicitly assumes that all electrons in the emission region contribute towards the afterglow emission. That may not be true and only a fraction $\xi_e$ of the total number of electrons may actually be shock accelerated into a power-law distribution to produce the observed synchrotron emission. In that case, a simple parametrization of $E \to E/\xi_e$, $n \to n/\xi_e$, $\epsilon_e \to \epsilon_e \xi_e$, and $\epsilon_B \to \epsilon_B \xi_e$ for $m_e/m_p < \xi_e < 1$ would yield the same spectral flux $F_\nu$ (Eichler & Waxman 2005). In this work, we assume $\xi_e = 1$.

## 3.2 Observer frame spectrum

The emission originates from a shocked layer of lab-frame width $\Delta = \Delta'/\Gamma \approx r/4(3-k)\Gamma^2$ and from polar angles $0 \leq \theta \leq \theta_j$, where $\theta$ is measured from the jet axis and $\theta_j$ represents the jet's semi-aperture. However, here we make a simplifying assumption and ignore the radial structure of the emitting volume and instead consider an infinitely thin-shell. This thin-shell is located at a normalized radial distance $\xi$ from the central source at the lab-frame time

$$t_{\text{lab}} = \frac{r_d}{c} \int_0^\xi \frac{d\xi'}{\beta(\xi')}, \qquad (17)$$

which depends on the dynamics through $\beta = \sqrt{1-\Gamma^{-2}} \approx 1 - 1/2\Gamma^2$ for $\Gamma \gg 1$. The direction to the observer, $\hat{n}$, is at an angle $\theta_{\text{obs}} = \cos^{-1}(\hat{n} \cdot \hat{z})$ from the jet axis, which we conveniently choose to point in the $\hat{z}$ direction (see Fig. 3). The arrival time $t$ to a distant observer of a photon emitted at radius $r$ and angle $\tilde{\theta} = \cos^{-1}(\hat{r} \cdot \hat{n})$ from the line-of-sight (LOS), from a source located at a redshift $z$ corresponding to a luminosity distance $d_L(z)$, is given by

$$t_z \equiv \frac{t}{(1+z)} = t_{\text{lab}} - \frac{r\tilde{\mu}}{c}, \qquad (18)$$

where $\tilde{\mu} = \cos\tilde{\theta} = \hat{r} \cdot \hat{n}$. When the observer is exactly along the jet's axis, $\hat{n} = \hat{z}$, $\theta_{\text{obs}} = 0$, and $\tilde{\theta} = \theta$.
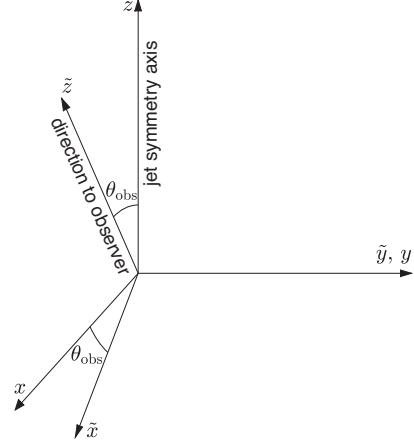


**Figure 3.** Coordinate system used to calculate the observed afterglow flux density and image. The $z$-axis is the outflow's symmetry axis, while the $\tilde{z}$-axis points to the observer and is in the $x$–$z$ plane at an angle of $\theta_{\text{obs}}$ from the $z$-axis. The $y$ and $\tilde{y}$ axes coincide. The afterglow image is in the plane of the sky, i.e. in the $\tilde{x}$–$\tilde{y}$ plane.

The spectral flux can be expressed using the isotropic comoving spectral luminosity $L'_{\nu'}$ such that (e.g. Granot 2005)

$$F_\nu(t) = \frac{(1+z)}{16\pi^2 d_L^2} \int \tilde{\delta}_D^3 L'_{\nu'} d\tilde{\Omega}, \qquad (19)$$

where $\tilde{\delta}_D = [\Gamma(1-\beta\tilde{\mu})]^{-1} \approx 2\gamma/(1+\Gamma^2\tilde{\theta}^2)$ for $\Gamma \gg 1$ is the Doppler factor and $d\tilde{\Omega} = d\tilde{\mu} d\tilde{\varphi}$ is the differential solid-angle subtended by the emitting region relative to the central source. It is clear from equation (18) that for a given observed time $t$, photons originating from different angles $\tilde{\theta}$, corresponding to angles $0 \leq \theta \leq \theta_j$, and radii $r$ contribute to the measured flux. Therefore, the integral over $d\tilde{\mu}$ in equation (19) must take into account the radiation arriving from an equal arrival time surface (e.g. Granot, Piran, & Sari 1999; Granot, Cohen-Tanugi, & Do Couto E Silva 2008), which relates $r$ and $\tilde{\mu}$ through equation (18) for a given $t_z$ and which extends radially from $\xi_{\text{min}}$ for $\tilde{\mu} = -1$ to $\xi_{\text{max}}$ for $\tilde{\mu} = 1$. For a given dynamical evolution of the shell these limiting radii can be obtained by finding the roots of the following equations:

$$\frac{ct_z}{r_d} = \left\{ \int_0^{\xi_{\text{min}}} \frac{1+\beta(\xi')}{\beta(\xi')} d\xi', \quad \int_0^{\xi_{\text{max}}} \frac{1-\beta(\xi')}{\beta(\xi')} d\xi' \right\}. \qquad (20)$$

In the early coasting stage, when $\Gamma(\xi) \approx \Gamma_0 \gg 1$, the above two limits simplify into $\{\xi_{\text{min}}, \xi_{\text{max}}\} \approx \{ct_z/2r_d, 2\Gamma_0^2 ct_z/r_d\}$.

In the thin-shell approximation, depending on the nature of the problem, the outer integral in equation (19) can either be performed over $\tilde{\mu} \in [-1, 1]$ or $\xi \in [\xi_{\text{min}}, \xi_{\text{max}}]$. In the latter case, integration over $\xi$ can be implemented with a simple calculation of the jacobian, such that $d\tilde{\mu} = |d\tilde{\mu}/d\xi| d\xi$, where

$$\tilde{\mu} = \frac{1}{\xi} \left[ \int_0^\xi \frac{d\xi'}{\beta(\xi')} - \frac{ct_z}{r_d} \right] \qquad (21)$$

$$\frac{d\tilde{\mu}}{d\xi} = \frac{1}{\xi^2} \left[ \frac{ct_z}{r_d} + \frac{\xi}{\beta(\xi)} - \int_0^\xi \frac{d\xi'}{\beta(\xi')} \right]. \qquad (22)$$

In order to perform the integral over the azimuthal angle $\tilde{\varphi}$, without loss of generality, the LOS is considered to lie in the $\hat{x}$–$\hat{z}$ plane ($\phi = 0$). This yields $\hat{n} = \hat{\tilde{z}} = \sin\theta_{\text{obs}}\hat{x} + \cos\theta_{\text{obs}}\hat{z}$, and the unit vectors spanning the plane of the sky (normal to the LOS), $\hat{\tilde{x}} = \cos\theta_{\text{obs}}\hat{x} - \sin\theta_{\text{obs}}\hat{z}$ and $\hat{\tilde{y}} = \hat{y}$. Then expressing any radial unit vector $\hat{r}$ in both coordinate systems and projecting it on to the

$\hat{z}$ axis yields the general relation

$$\cos\left[\tilde{\varphi}(\tilde{\mu},\mu,\mu_{\text{obs}})\right] = \frac{\tilde{\mu}\mu_{\text{obs}} - \mu}{\sqrt{(1-\tilde{\mu}^2)(1-\mu^2)}}. \tag{23}$$

For a spherical flow, the properties of the emission donot depend on $(\tilde{\mu}, \tilde{\varphi})$, and therefore the observer receives emission from $\Delta\tilde{\varphi} = 2\pi$.

### 3.3 Comparison of afterglow light curves with observations of GRB 170817a

Here, we compare the prediction of the light curves obtained for the structured jets (e.g. Granot & Kumar 2003; Kumar & Granot 2003; Rossi et al. 2004; Lamb & Kobayashi 2017; Salafia, Ghisellini & Ghirlanda 2018) and the (quasi-) spherical outflows (e.g. Fraija & Veres 2018; Gottlieb, Nakar, & Piran 2018; Hotokezaka et al. 2018; Salafia et al. 2018) to the radio (3 and 6 GHz), optical (at 2 eV), and X-ray (at 1 keV) observations of SGRB 170817A (e.g. Margutti et al. 2018; Alexander et al. 2018; Rossi et al. 2018). The first X-ray and radio detections are at 8.9 d and 16.4 d, respectively, and the observed flux density at these wavelengths appears to be dominated by the afterglow emission throughout all of the observations so far. However, during the first few weeks the observed flux density in the optical (as well as in the IR and the early UV emission) is dominated by the kilonova emission. Therefore, in order to avoid any significant contribution of the kilonova component that is not included in our modelling, we use the optical observations only at sufficiently late times (Lyman et al. 2018; Margutti et al. 2018) for fitting the simulated light curves. Furthermore, all these observations, that were obtained between ∼9 and ∼163 d post merger, suggest that the afterglow radio to X-ray emissions lie on the same synchrotron power-law segment [PLS – specifically PLS G as discussed in Granot & Sari (2002)]. This fact offers a way to constrain some of the parameters in the large parameter space of the models considered here. Therefore, all the light curves that are shown below respect the constraint that $\nu_{\text{m}} < 3$ GHz and $h\nu_{\text{c}} > 10$ keV over the entire period over which the afterglow data was obtained.

In the first row of Fig. 4, we show the afterglow light curves from the GJ and PLJ models. In both cases, the jet has a narrow core with $\theta_{\text{c}} \sim 5°$ and the viewing angle is $\theta_{\text{obs}} \sim 27°$. We stress that these are tentative fits to the data, which are by no means unique, and other sets of model parameters may provide a comparably good fit. None the less, they are still representative for most purposes. In the second row of Fig. 4, we show the light curves for the Sph and QSph models. For these, we find that the values of $s$ are similar to the expected ones (compare to Appendix A1). For the PLJ model, we obtain a value of $a = 4.5$, and generally find that $a \gtrsim 3.5-4$ is preferred by the afterglow data. This is significantly larger than the $a \approx 2.7$ that is inferred from the asymptotic analytic estimate in Appendix A2. However, this is likely due to the fact that in our case $\theta_{\text{obs}}/\theta_{\text{c}} = 5.4$ does not quite allow to reach the asymptotic range of $\theta$-values, $\theta_{\text{c}} < \theta \ll \theta_{\text{obs}}$, for which that analytic estimate was calculated.

The (asymptotic) temporal index of $F_\nu(t)$, $\alpha \equiv d\log F_\nu/d\log t$ is derived for a power-law $E_{\text{k,iso}}(> u) \propto u^{-s}$ radial energy injection and for a jet with a narrow core and power-law wings in Appendices A1 and A2, respectively. Fig. 5 shows $\alpha(t)$ of the light curves from our tentative fits to the data. At early times, when the outflow is in the coasting phase, $F_\nu \propto R^3 \propto t^3$. After the flow decelerates, marked by the decrease in the temporal index, the slight curvature in the light curves for $10 \text{ d} \lesssim t \lesssim 100 \text{ d}$ is apparent. The light curves in all models reach the peak at approximately the same time

at $t_{\text{p}} \sim 150$ d (also see Dobie et al. 2018; Margutti et al. 2018). For $t > t_{\text{p}}$, the temporal index of the two structured jet models is steeper than that of any wide-angle quasi-spherical flow. This can potentially serve as a discriminator between the two types of jet profiles. For $t \gtrsim 10^3$ d, the counter-jet starts to contribute to the flux and produces a flattening in the light curves. Numerical simulations suggest that the counter-jet may have a stronger effect on the light curve when it becomes visible (De Colle et al. 2012; Granot, De Colle & Ramirez-Ruiz 2018).

In the case of structured jets, for which our fit parameters are very similar for the GJ and PLJ models, we compare our results to the fit parameters obtained using magnetohydrodynamic simulations in recent works. In Lazzati et al. (2017b), the best-fitting parameters are: $\theta_{\text{obs}} \sim 33°$, $\theta_{\text{c}} \sim 1°$, $E_{\text{iso,c}} \sim 10^{52}$ erg, $\Gamma_{\text{c}} \approx 80$, $n_0 \sim 4 \times 10^{-3}$ cm$^{-3}$, $\epsilon_{\text{e}} \approx 6 \times 10^{-2}$, $\epsilon_{\text{B}} \approx 3.3 \times 10^{-3}$, and $p \approx 2.07$. Likewise, in Margutti et al. (2018), the best-fitting parameters (for one of their models) are: $\theta_{\text{obs}} = 20°$, $\theta_{\text{c}} \sim 9°$, $E_{\text{iso,c}} \sim 10^{53}$ erg, $\Gamma_{\text{c}} \approx 10^2$, $n_0 = 10^{-4}$ cm$^{-3}$, $\epsilon_{\text{e}} = 2 \times 10^{-2}$, $\epsilon_{\text{B}} = 10^{-3}$, and $p = 2.16$. On the other hand, for the wide-angle flow scenario explored by Mooley et al. (2018), one of their models, which is somewhat closer to the QSph model explored in this work, yields the following best-fitting parameters: $u_{0,\text{min}} = 1$, $u_{0,\text{max}} = 3.5$, $s = 5$, $E_{\text{iso}} = 2 \times 10^{51}$ erg, $n_0 = 8 \times 10^{-5}$ cm$^{-3}$, $\epsilon_{\text{e}} = 10^{-2}$, $\epsilon_{\text{B}} = 10^{-1}$, and $p = 2.2$. In a recent work, Resmi et al. (2018) conducted an MCMC maximum likelihood analysis using a semi-analytic model of a Gaussian jet, much similar to the GJ model presented here, and obtained the following fit parameters: $E_{\text{k,iso,c}} = 10^{51.76}$ erg, $\Gamma_{\text{c}} = 215$, $\theta_{\text{c}} = 6.9°$, $\theta_{\text{obs}} = 27°$, $n_0 = 10^{-2.68}$ cm$^{-3}$, $\epsilon_{\text{e}} = 10^{-0.66}$, $\epsilon_{\text{B}} = 10^{-4.37}$, and $p = 2.17$. These model parameters are consistent with our results.

## 4 LINEAR POLARIZATION

The degree of linear polarization depends on the orientation of the magnetic field with respect to the LOS and its coherence length when compared with the angular size of the visible region, i.e. $\theta \sim 1/\Gamma$. An ordered magnetic field with a large coherence length can give rise to a large degree of linear polarization $\Pi$ (Granot 2003; Granot & König 2003). A more random magnetic field with a smaller coherence length would produce a smaller $\Pi$. A completely random field in 3D produces no net polarization even locally (over a region much larger than its coherence length but much smaller than the size of the emitting region). A completely random magnetic field in the plane of the shock produces local polarization in different parts of the image, but for a spherical flow it averages out to zero over the whole image (for an unresolved source such an effective averaging cannot be avoided) leaving no net linear polarization ($\Pi = 0$). In this case, the axial symmetry around our line of sight needs to be broken. In our case this happens if the flow is axisymmetric and our viewing angle is offset (by an angle $\theta_{\text{obs}} > 0$) relative to the flow's symmetry axis. This has been studied for a uniform jet with sharp edges that is viewed off-axis (e.g. Sari 1999; Ghisellini & Lazzati 1999), or for an outflow with more angular structure, viz. $\epsilon(\theta)$ and/or $\Gamma(\theta)$ viewed off-axis (e.g. Rossi et al. 2004).

Here, we consider a random magnetic field that is tangled on angular scales $\ll 1/\Gamma$, with axial symmetry with respect to the shock normal $\hat{n}_{\text{sh}}$. The field anisotropy is parametrized by $b \equiv 2\langle B_\parallel^2\rangle/\langle B_\perp^2\rangle$, where $B_\parallel$ ($B_\perp$) is the magnetic field component parallel (perpendicular) to $\hat{n}_{\text{sh}}$ (Granot & König 2003). In this case the local polarization in the comoving frame around the LOS is
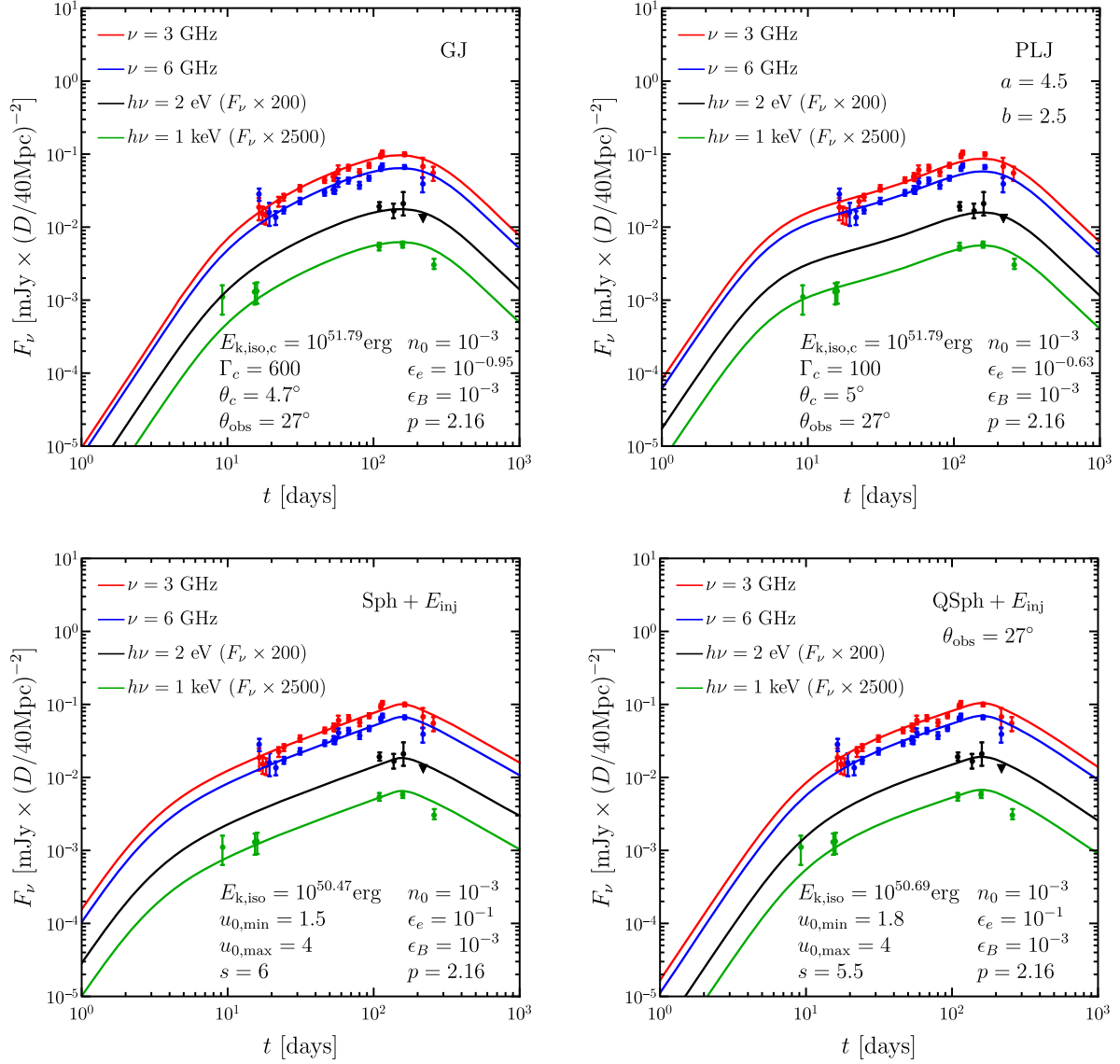
**Figure 4.** Comparison of radio, optical, and X-ray light curves for the Gaussian jet (GJ; top left, with total energy $E_{\rm tot} = 4.22 \times 10^{49}$ erg), power-law jet (PLJ; top right, $E_{\rm tot} = 1.9 \times 10^{49}$ erg), spherical shell with energy injection (Sph; bottom left, $E_{\rm tot} = 2.95 \times 10^{50}$ erg), and quasi-spherical shell with energy injection (QSph; bottom right, $E_{\rm tot} = 1.93 \times 10^{50}$ erg) to the afterglow data for GRB 170817A.
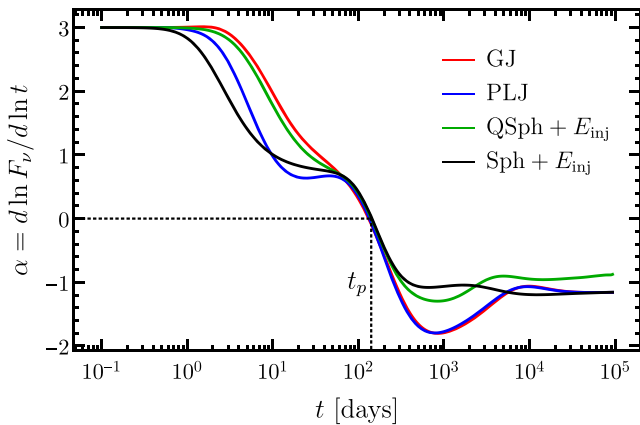


**Figure 5.** Temporal index of the light curves shown for the GJ, PLJ, QSph, and Sph models.

given by (Gruzinov 1999; Sari 1999)

$$\Pi(\tilde{\theta}') = \Pi_{\max} \frac{(b-1)\sin^2(\tilde{\theta}')}{2 + (b-1)\sin^2(\tilde{\theta}')} \quad \text{with} \quad \Pi_{\max} = \frac{p+1}{p+7/3}, \quad (24)$$

where $\Pi_{\max} \simeq 0.7$ for $p = 2.16$. For $b > 1$ ($b < 1$), the local polarization is $\Pi > 0$ ($\Pi < 0$) and the direction of the polarization vector is along (normal to) the direction of $\hat{n} \times \hat{n}_{\rm sh}$. The polar angles in the comoving frame can be related to that in the lab frame through the aberration of light

$$\tilde{\mu}' = \frac{\tilde{\mu} - \beta}{1 - \beta\tilde{\mu}}. \quad (25)$$

Recall that the local dynamics depend on the polar angle from the jet symmetry axis, so that $\beta = \beta(\theta, r) = \beta(\tilde{\mu}, \tilde{\phi}, r)$. The degree of polarization can be conveniently expressed using the Stokes parameters, which are obtained by averaging over the polarization
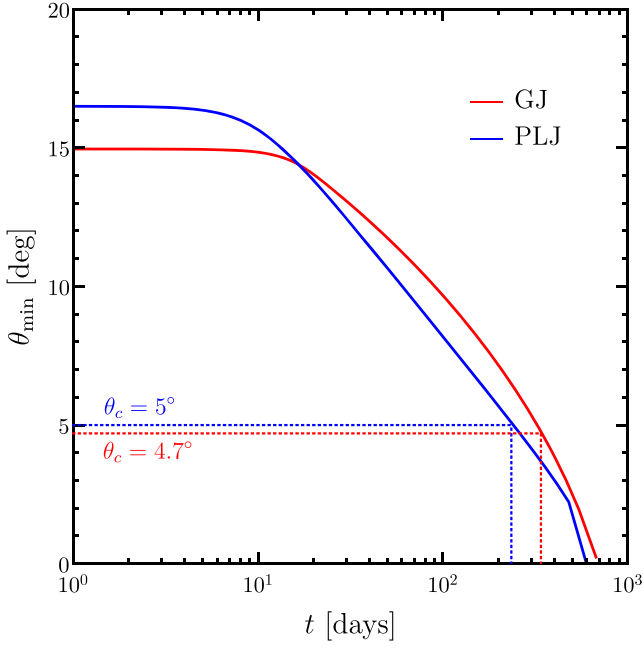
**Figure 6.** Minimum angle from which the emission contributes to the flux in the LOS.

emerging from each fluid element in the visible region, such that

$$
\left\{ \begin{matrix} Q/I \\ U/I \end{matrix} \right\} = \frac{\int \tilde{\delta}_{\mathrm{D}}^3 L'_{\nu'} \Pi \left\{ \begin{matrix} \cos 2\tilde{\phi} \\ \sin 2\tilde{\phi} \end{matrix} \right\} \mathrm{d}\tilde{\Omega}}{\int \tilde{\delta}_{\mathrm{D}}^3 L'_{\nu'} \mathrm{d}\tilde{\Omega}}. \tag{26}
$$

The degree of polarization is obtained from $\Pi = \sqrt{Q^2 + U^2}/I$, where $I \propto F_\nu$.

Let us first consider a structured jet, either GJ or PLJ. In this case, $\Pi$ rises with time as emission from more energetic regions at $\theta < \theta_{\mathrm{obs}}$ comes into view. The local beaming cone has a half-opening angle $\theta_b = \arccos \beta$ that approaches $1/\Gamma$ for $\Gamma \gg 1$. In Fig. 6, we show the minimum polar angle $\theta_{\mathrm{min}}$ from the jet symmetry axis the beaming cone of which just includes the LOS, i.e. when $\theta_{\mathrm{obs}} - \theta_{\mathrm{min}} = \theta_b(\theta_{\mathrm{min}}) = \arccos \beta \approx 1/\Gamma(\theta_{\mathrm{min}})$, which in the relativistic regime corresponds to $\Gamma(\theta_{\mathrm{min}})(\theta_{\mathrm{obs}} - \theta_{\mathrm{min}}) \approx 1$. Initially, at early times during the coasting phase ($t \lesssim 10\,\mathrm{d}$ in our case) $\theta_{\mathrm{min}}$ assumes a constant value. Over time, as the faster moving parts of the jet slow down and their beaming cones widen, $\theta_{\mathrm{min}}$ gradually decreases and moves closer to $\theta_c$. Since most of the energy resides at $\theta \lesssim \theta_c$, the level of polarization peaks, as shown in the left-hand panel of Fig. 7, near the time when $\theta_c$ becomes visible to the observer (around ~300 d or so in our case). This is a factor of ~2 after the peak of the light curve, $t_{\mathrm{p}}$, since a rise in flux in such an angular scenario requires a sufficiently fast increase in the energy within the visible region (see Appendix A2), but $\epsilon(\theta)$ starts to level off already somewhat above $\theta_c$ so that the flux peaks and starts to decay when $\theta_{\mathrm{min}}$ is still somewhat larger than $\theta_c$. Such an effect is not seen for the quasi-spherical model, where the time of the peak in the light curve and in the polarization practically coincide.

The degree of polarization starts to decline as the observed flux is dominated by the jet's core, which continues to decelerate so that the photons that reach us are emitted closer to the shock normal in the comoving frame (at smaller $\theta'$), which reduces $\Pi(\theta')$ (see equation 24). The polarization and its time evolution, $\Pi(t)$, is very similar for our two off-axis structured jet models.

The linear polarization, in particular near the time of the peak in the light curve, is much larger for an off-axis jet whose energy is dominated by its narrow core, compared to a quasi-spherical flow. However, the degree of polarization for all outflow structures considered here could decrease by about the same factor if in reality the magnetic field behind the afterglow shock is not random only fully within the plane of the shock ($b = 0$) (e.g. Sari 1999; Granot 2003; Granot & Königl 2003), but also has a comparable random component in the direction of the shock normal ($b > 0$). This might be hinted by the relatively low levels of linear polarization usually measured in GRB afterglows in the optical or NIR (of $\Pi \lesssim$ a few per cent, e.g. Covino & Götz 2016). Therefore, a potentially more robust difference between the expected $\Pi(t)$ for these different outflow models is its time evolution – for our off-axis jets there is a more distinct peak in $\Pi(t)$ near the time of the peak in the light curve, $t_{\mathrm{p}}$.

The polarization vector on the plane of the sky is expected to be along the $\tilde{x}$-axis (which is also along the direction of motion of the flux centroid) for $0 \le b < 1$, and along the $\tilde{y}$-axis (which is normal to the direction of motion of the flux centroid) for $b > 1$.

## 5 THE RADIO IMAGE – FLUX CENTROID, SIZE, AND SHAPE

Possibly the most promising way to break the degeneracy between the models considered in this work is by comparing the properties of the image on the plane of the sky, especially in radio (see e.g. Granot & van der Horst 2014, for a review), to that obtained from the various models. Several properties of the radio image can potentially be directly compared with observations, depending on whether and how well the image is resolved. Another important diagnostic that can help break the degeneracy between different outflow models is the motion of the flux centroid (e.g. Sari 1999; Granot & Loeb 2003), which may in some cases be detected even if the image is only marginally resolved or even not resolved altogether.

In order to calculate the flux centroid, we consider the image of the outflow on the plane of the sky with coordinates $(\tilde{x}, \tilde{y})$, where the line connecting the LOS to the jet symmetry axis coincides with the $\tilde{x}$-axis. The image will always be symmetric around this line, and therefore the flux centroid will move along the $\tilde{x}$-axis. The position of the flux centroid $\tilde{x}_{\mathrm{fc}}(t)$, expressed in terms of the angular displacement $\theta_{\mathrm{fc}}(t)$ from the location of the GRB central source, is simply an average of $\tilde{x} = \tilde{\rho} \cos \tilde{\phi} = R\sqrt{1 - \tilde{\mu}^2} \cos \tilde{\phi}$ weighted by $F_\nu$, such that

$$
\tilde{x}_{\mathrm{fc}}(t) = \frac{\int \delta_{\mathrm{D}}^3 L'_{\nu'} \tilde{\rho} \cos \tilde{\phi}\, \mathrm{d}\tilde{\Omega}}{\int \delta_{\mathrm{D}}^3 L'_{\nu'}\, \mathrm{d}\tilde{\Omega}} \quad \text{and} \quad \theta_{\mathrm{fc}}(t) \equiv \frac{\tilde{x}_{\mathrm{fc}}}{d_{\mathrm{A}}} \approx \frac{\tilde{x}_{\mathrm{fc}}}{d}, \tag{27}
$$

where $d_{\mathrm{A}} = (1 + z)^{-1}$, $d_{\mathrm{A}}$ is the angular distance and $d$ is the proper distance, and $d_{\mathrm{A}} \approx d$ when $z \ll 1$; we use $d = 40\,\mathrm{Mpc}$ for GRB 170817A.

In the right-hand panel of Fig. 7, we show the motion of the flux centroid for all the models considered in this work. The angular position of the flux centroid evolves in a similar way for the GJ and PLJ models. However, its evolution is very different for the QSph model (for the Sph model it obviously does not move at all). The maximum $\theta_{\mathrm{fc}}(t)$ for the QSph model is significantly lower than that predicted for the two structured jets, and it peaks (i.e. its movement reverses direction) at a slightly earlier time compared with GJ and PLJ models. For the GJ and PLJ models, $\theta_{\mathrm{fc}}(t)$ peaks
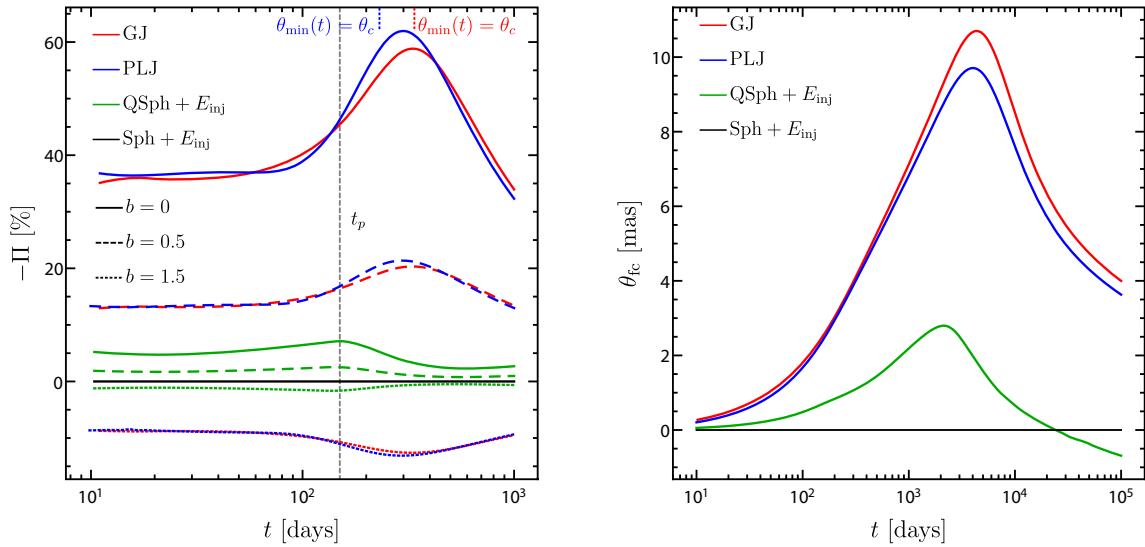
**Figure 7.** (Left) Linear polarization in radio at 3 GHz for the different models shown in this work. The degree of polarization for different levels of magnetic field anisotropy is shown, where for $b = 0$ (solid) the field is completely in the plane perpendicular to the shock normal, and for $b = 0.5$ (dashed) and $b = 1.5$ (dotted) the field component in the direction of the shock normal also contributes. For $b = 1$ both components contribute equally, which yields no net polarization. Between the two cases where $b < 1$ and $b > 1$, the polarization position angle changes direction by $90°$. The times at which emission from the jet core ($\theta = \theta_c$) starts contributing to the flux are indicated with dotted lines. The peak time of the light curves $t_p$ is shown with a grey vertical dashed line. (Right) Angular separation of the flux centroid (in milliarcsecond) from the centre of the GRB.

around the time when the jet's core becomes sub-relativistic and the counter-jet's core becomes visible.

In Figs 8 and 9, we show the radio images on the plane of the sky for the GJ, PLJ, QSph, and Sph models (also see Nakar et al. 2018). The specific intensity $I_\nu$ is normalized by its mean value within the image, $\langle I_\nu \rangle$, and these normalized images are independent of frequency within the same spectral PLS, and are shown here for PLS G where $I_\nu$, $F_\nu \propto \nu^{(1-p)/2}$. Since the emission is from a thin shell, the images are particularly limb brightened and $I_\nu$ diverges near the outer edge of the image as the square root of the projected distance from the edge (Sari 1998; Granot & Loeb 2001; Granot 2008). When the emission from the bulk of the hot plasma behind the afterglow shock is considered, the resulting images are somewhat less limb brightened, and the surface brightness no longer diverges and instead peaks at a lower value somewhat before the outer edge of the image (Granot, Piran, & Sari 1999; Granot & Loeb 2001; Granot 2008). However, for PLS G with $p = 2.2$, $I_\nu$ within the circular image for the Blandford & McKee (1976) self-similar solution peaks at 95 per cent of its outer radius, and the overall limb brightening is not that different from PLS H for which the emission is indeed from a very thin cooling layer just behind the shock (see fig. 2 of Granot 2008).

At early times, the emission from the main jet dominates the intensity and observed flux, and therefore determines the location of the flux centroid, while emission from the counter-jet is beamed away from the observer. At late times, when the counter-jet's core becomes sub-relativistic the counter-jet's contribution to the observed flux becomes more prominent and it starts moving the flux centroid back towards the location of the central source.

We show the evolution of the mean size of the radio images and its axial ratio over time in Fig. 10. The difference in the angular size near the peak of the light-curve $t_p$ between the different models is rather modest ($\lesssim 25$ per cent), and even at very late times

it is a factor of $\lesssim 2$. Therefore, this may not be the best way to distinguish between the different models. However, the image axis ratio, which parametrizes its degree of elongation may be a better and more robust way to distinguish between the two main types of models (GJ or PLJ versus QSph or Sph). For the (quasi-) spherical model, the image is (almost) circular, while for the off-axis structured jet models the image is rather elongated with an axis ratio of $\gtrsim 2$ near $t_p$, and even somewhat more elongated at later times.

Since GRBs are usually cosmological sources and their afterglow images may at best be only marginally resolved, it is challenging to measure the actual angular size or shape of the outflow from radio observations. Instead the visibility data is fit to an assumed parametrized image surface brightness distribution. The surface brightness of these sources is often modelled as a circular or an elliptical Gaussian (e.g. Taylor et al. 2005; Taylor & Granot 2006; Pihlström et al. 2007; Mesler et al. 2012). The results of such a fit may be biased due to the inhomogeneous brightness profile of the outflow, if it is significantly different than the assumed functional form. Therefore, the outflow sizes inferred from e.g. radio images of GRBs may potentially be somewhat smaller than their true full sizes (e.g. Taylor et al. 2004; Pihlström et al. 2007).

Our simplified dynamics may introduce some differences in the resulting afterglow images compared to more realistic full hydrodynamic simulations. Our neglect of the lateral jet dynamics affects mainly our jet models (our spherical model does not suffer from this problem, and the expected effects for the quasi-spherical model are also rather modest). It may render the results less realistic at late times, especially when the flow becomes Newtonian and is expected to approach the spherical self-similar Sedov–Taylor solution. Therefore, the relatively large image axis ratio at very late times, well after the jet's core becomes sub-relativistic at $t_{NR} \sim 2-3$ yr, is likely to be more modest and gradually decrease with time rather than increase with time as the flow becomes more spherical and
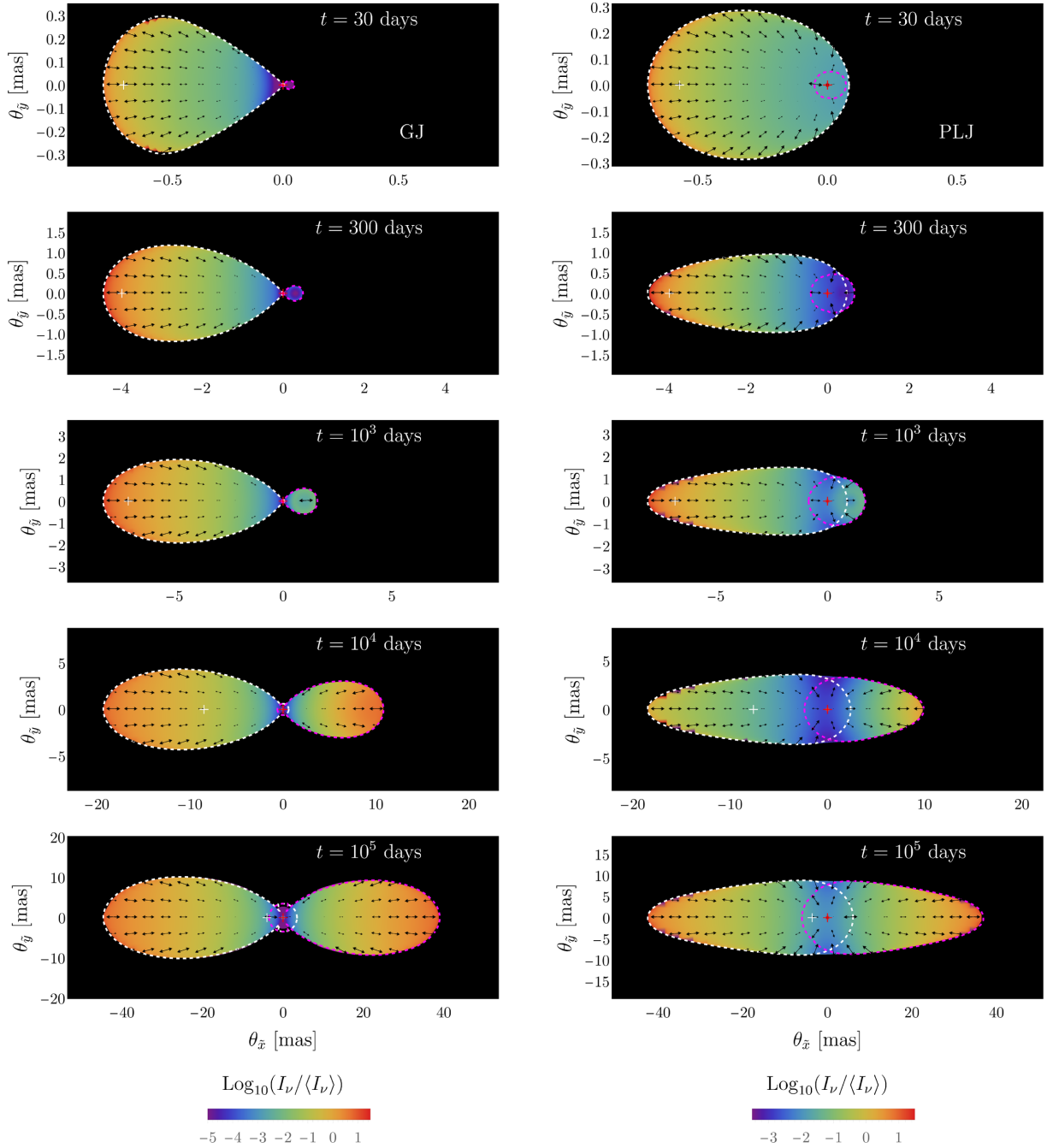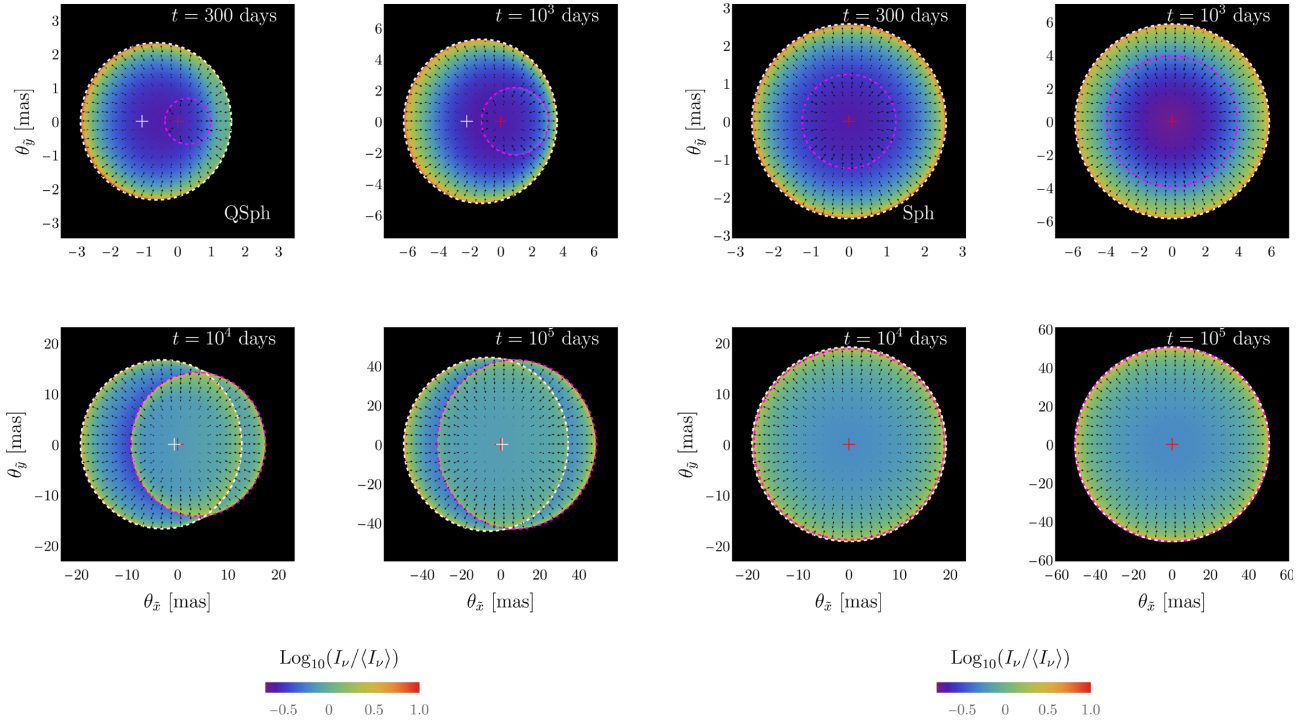
**Figure 8.** Radio afterglow images of the outflow on the plane of the sky with polarization maps for the two different models discussed in this work: a Gaussian jet (GJ; left-hand panels) and a core+power-law jet (PLJ; right-hand panels). These normalized images are independent of frequency within the same spectral PLS, and are shown here for PLS G where $F_\nu \propto \nu^{(1-p)/2}$. The maximum extents of the main and counter jets are shown with white and magenta dotted lines, respectively. The location of the GRB central source is marked with a red '+'-sign and the position of the flux centroid is marked with a white '+'-sign. The polarization vectors are shown with double-sided black arrows, whose length scales linearly with the degree of polarization.

Newtonian at such late times. It is more reasonable to expect the image axis ratio to peak at $\sim 2-3$, around $t_{NR}$, and then gradually decrease.

An accompanying paper (Granot et al. 2018) presents afterglow images from 2D relativistic hydrodynamic simulations of an initially conical jet with sharp edges. One can get a better idea of the expected differences between our simplified dynamics and hydrodynamic simulations by a comparison with those results, despite the different initial jet structure. For our simplified dynamics the jet's

non-relativistic transition radius $R_{NR}$ and corresponding observer time $t_{NR} \sim R_{NR}/c$ is given by the Sedov radius corresponding to $E_{k,iso}(\theta = 0)$. Alternatively one can estimate it for semi-analytic models featuring exponential lateral expansion at $R > R_j$ where the jet break radius $R_j$ is approximately the Sedov radius corresponding to the jet's true energy, which gives $R_{NR} \approx (1 - \ln \theta_0)R_j$. The ratio of the latter and former radii is $\theta_0^{2/(3-k)}(1 - \ln \theta_0)$ which for $\theta_0 = 0.2$ gives 0.89 for a uniform density ($k = 0$) but 0.10 for a wind-like external density profile ($k = 2$). While simulations give a

**Figure 9.** Radio afterglow images of the outflow on the plane of the sky with polarization maps for the quasi-spherical shell (QSph; left) and spherical shell (Sph; right) with energy injection models. The format is the same as in Fig. 8.
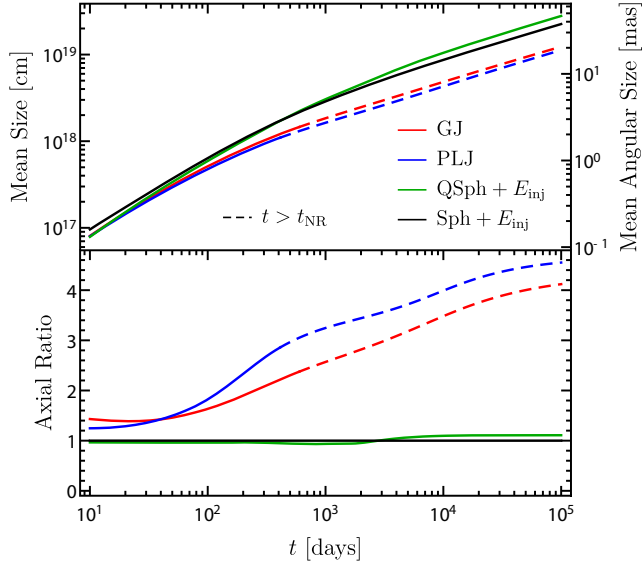


**Figure 10.** (Top) Geometric mean size of the image (half of the total image extent in the $\tilde{x}$ and $\tilde{y}$ directions). (Bottom) Axial ratio of the image. The dashed line shows the mean size and axial ratio at times after the main jet becomes non-relativistic ($t > t_{NR}$) for the GJ and PLJ models. Due to the simple lateral dynamics (no lateral spreading) assumed in this work, the predictions for the size and axial ratio may not be so robust.

result closer to the latter radius for a wind-like density profile, for the purposes of this work a uniform density is relevant, for which there are very small differences between these two estimates, so that our results should be quite reasonable. For a uniform density

this time and radius scale as $t_{NR} \sim R_{NR}/c \propto (E/n)^{1/3}$ with the jet energy and external density. The angular scale of the image around this time is $\sim\theta_{NR} = R_{NR}/d$.

For the hydrodynamics presented in Granot et al. (2018), the counter jet dominates the observed flux just after it becomes visible, causing the flux centroid to move to the other side of the central source, reaching a maximum displacement on that (counter-jet's) side a factor of $\sim 2$ in time after it passes through the projected location of the central source ($\tilde{x} = 0$), and then gradually moves back towards it at late times as the contribution of the main and counter jets becomes closer to each other. In this work, the effect of the counter jet is smaller, and it never quite dominates the flux. This likely occurs due to the more gradual deceleration of the jet's core in our simplified dynamics. A similar trend appears for a wind-like external density profile in the simulations (De Colle et al. 2012), for which the jet decelerates more slowly.

## 6 DISCUSSION AND CONCLUSIONS

The broad-band afterglow light curve of GRB 170817A that continues to rise even $\gtrsim 115$ d post merger has seriously challenged the naive view that outflows in GRBs are narrowly beamed and have sharp edges, with perhaps a homogeneous angular profile. Such a picture is also inconsistent with the sub-luminous prompt gamma-ray emission of GRB 170817A (e.g. Granot, Guetta & Gill 2017), which appears to arise from material along our line of sight. Model fits to radio and X-ray observations have revealed that the rising flux of GRB 170817A can be explained by two completely distinct models, namely a structured jet and a quasi-spherical outflow with initial radially stratified velocity profile. In terms of the light

curves, both types of models can explain the current observations. The predicted flux decay after the peak in the light curve is somewhat steeper for the off-axis structured jet models compared to the (quasi-) spherical models (see Figs 4 and 5), but this may still not suffice to clearly distinguish between these models. Therefore, new types of diagnostics are needed to break this degeneracy.

In this work, we present three different diagnostics that appear to be most promising and may also be observationally feasible, which may help to unveil the true nature of the outflow that powered GRB 170817A:

(i) *Polarization*: The degree of polarization ($\Pi$) for the structured jets, namely the GJ and PLJ models, undergoes a sharp increase beyond $\sim 100$ d and peaks at $\sim 300$ d, where $\Pi \approx 60$ per cent (for $b = 0$). This trend is in stark contrast with any wide-angle quasi-spherical flow for which $\Pi \lesssim 10$ per cent. Radio or optical measurements of the afterglow polarization may help distinguish between the structured jet and the 'cocoon' scenario [also see e.g. D'Avanzo et al. (2018); Nakar et al. (2018)]. A caveat here is that high $\Pi$-values assume a magnetic field that is fully random within the shock plane ($b = 0$), in 2D, while a field that is partly random in 3D and also has a comparable component in the direction of the shock normal ($b > 0$) could potentially significantly reduce $\Pi$, by a similar factor for these different models. Another potential diagnostic may be obtained by comparing the peak time $t_\pi$ for $\Pi(t)$ and $t_p$ for $F_\nu(t)$: for the GJ and PLJ models $t_\pi/t_p \approx 2$ while for a wide-angle quasi-spherical flow $t_\pi/t_p \approx 1$.

(ii) *Flux centroid motion*: A potentially powerful diagnostic is the motion of the flux centroid in relation to the location of the GRB (that corresponds to the flux centroid's location at very early or late times). Both the GJ and PLJ models show a large displacement of the flux centroid (reaching $\sim 3$ mas at $\sim 200$ d) due to the modest viewing angle and the inherent angular profile of the outflow. On the other hand, a lower offset ($\lesssim 1$ mas at $\sim 200$ d) is expected from any quasi-spherical flow.

(iii) *Axial ratio of the image*: The size of the image and its axial ratio, which may be determined using VLBI, can be instrumental in discerning the properties of the outflow (see e.g. Taylor et al. 2005; Taylor & Granot 2006; Pihlström et al. 2007; Mesler et al. 2012). We find that all the models that are considered in this work and fit $F_\nu(t)$ the predicted image sizes as a function of time are approximately similar. This makes it challenging to differentiate between the different models. However, the axial ratio can serve as an important discriminator between a structured jet and quasi-spherical outflow at the current epoch. On the other hand, the difference in the axial ratio between the GJ and PLJ models is $\lesssim 25$ per cent, which remains approximately at that level even at late times. This makes it harder to distinguish between the two jet profiles.
The axial ratio for any wide-angle flow remains very close to unity at all times, while for the structured jets the axial ratio is $\sim 2$ at $\sim 200$ d.

A high angular resolution instrument is needed to resolve the image and measure the flux centroid's movement, even for GRB 170817A that is at a relatively nearby distance of $\approx 40$ Mpc. The relatively small distance required for detecting binary mergers in gravitational waves is also more favourable for imaging compared to cosmological GRBs. In order to break the degeneracy between our structured jets and quasi-spherical models for GRB 170817A at $\sim 200$ d, a minimum angular resolution of $\approx 2$ mas is needed. This is within reach of the VLBA network in the Northern hemisphere, where using the longest baseline there of 8008 km between the Effelsberg and the Jansky Very Large Array (JVLA) site in New Mexico, the minimum angular resolution is $\sim 170\,\mu$as at 43 GHz or $\approx 1.5$ mas at 5 GHz. Since observations of GRB 170817A show that the flux density falls off with frequency as $F_\nu \propto \nu^{-0.6}$, it may not be possible to realize in practice the higher theoretical angular resolution at higher frequencies, and instead it might be required to opt for lower frequencies despite the lower corresponding possible angular resolution, because of the higher $F_\nu$ that may hopefully enable to actually image and resolve the source in practice. The motion of the flux centroid may potentially be determined to somewhat better accuracy, and may possibly be measured even if the image is not resolved.

Linear polarization of GRB afterglow emission mostly at the $\sim 1-2$ per cent level has been obtained for several GRBs in the optical or NIR, but only upper limits were obtained in radio (e.g. Covino & Götz 2016). The detection of polarization depends on the sensitivity of the instrument and the flux of the source, which together yields a measure of signal-to-noise ratio (SNR). A high SNR is typically needed to register any polarization. Therefore, it may be challenging to measure the afterglow polarization for GRB 170817A.

In this work, we provide clear predictions for the afterglow light curves, polarization, and image properties for the four different outflow models that can explain the observed flux evolution from radio to X-rays. Broad-band observations in the near future may be able to distinguish between structured jet and quasi-spherical outflow models for GRB 170817A. This can take us one step closer to unraveling the nature of the outflows in GRBs.

## REFERENCES

Abbott B. P. et al., 2017a, Phys. Rev. Lett., 119, 161101
Abbott B. P. et al., 2017b, ApJ, 848, L12
Abbott B. P. et al., 2017c, ApJ, 848, L13
Alexander D. et al., 2018, preprint (arXiv:1805.02870)
Alexander K. D. et al., 2017, ApJ, 848, L21
Blandford R. D., McKee C. F., 1976, Phys. Fluids, 19, 1130
Chevalier R. A., Li Z.-Y., 2000, ApJ, 536, 195
Chevalier R. A., Li Z.-Y., Fransson C., 2004, ApJ, 606, 369
Chornock R. et al., 2017, ApJ, 848, L19
Coulter D. A. et al., 2017, Science, 358, 1556
Covino S., Götz D., 2016, A&AT, 29, 205
Covino S. et al., 2017, NatAs, 1, 791
Cowperthwaite P. S. et al., 2017, ApJ, 848, L17
De Colle F., Ramirez-Ruiz E., Granot J., Lopez-Camara D., 2012, ApJ, 751, 57
Dobie D. et al., 2018, ApJ, 858, L15
Drout M. R. et al., 2017, Sci, 358, 1570
D'Avanzo P. et al., 2018, A&A, 613, L1
Eichler D., Waxman E., 2005, ApJ, 627, 861
Fraija N., Veres P., 2018, preprint (arXiv:1803.02978)
Garcia-Segura G., Langer N., Mac Low M.-M., 1996, A&A, 316, 133
Ghisellini G., Lazzati D., 1999, MNRAS, 309, L7
Goldstein A. et al., 2017, ApJ, 848, L14
Gottlieb O., Nakar E., Piran T., 2018, MNRAS, 473, 576
Granot J., 2003, ApJ, 596, L17
Granot J., 2005, ApJ, 631, 1022
Granot J., 2008, MNRAS, 390, L46

Granot J., Cohen-Tanugi J., Do Couto E Silva E., 2008, ApJ, 677, 92

Granot J., De Colle F., Ramirez-Ruiz E., 2018, preprint (arXiv:1803.05856)

Granot J., Guetta D., Gill R., 2017, ApJ, 850, L24

Granot J., Kumar P., 2003, ApJ, 591, 1086

Granot J., Königl A., 2003, ApJ, 594, L83

Granot J., Loeb A., 2001, ApJ, 551, L63

Granot J., Loeb A., 2003, ApJ, 593, L81

Granot J., Piran T., Sari R., 1999, ApJ, 513, 679

Granot J., Sari R., 2002, ApJ, 568, 820

Granot J., van der Horst A. J., 2014, PASA, 31, 8

Gruzinov A., 1999, ApJ, 525, L29

Haggard D., Nynka M., Ruan J. J., Kalogera V., Cenko S. B., Evans P., Kennea J. A., 2017, ApJ, 848, L25

Hallinan G. et al., 2017, Sci, 358, 1579

Hotokezaka K. et al., 2018, preprint (arXiv:1803.00599)

Kasliwal M. M. et al., 2017, Science, 358, 1559

Kouveliotou C. et al., 2013, ApJ, 779, L1

Kumar P., Granot J., 2003, ApJ, 591, 1075

Kyutoku K., Ioka K., Shibata M., 2014, MNRAS, 437, L6

Lamb G. P., Kobayashi S., 2017, MNRAS, 472, 4953

Lamb G. P., Kobayashi S., 2018, MNRAS, 478, 733

Lazzati D., Deich A., Morsony B. J., Workman J. C., 2017a, MNRAS, 471, 1652

Lazzati D. et al., 2017b, preprint (arXiv:1712.03237)

Lyman J. D. et al., 2018, preprint (arXiv:1801.02669)

Margutti R. et al., 2017, ApJ, 848, L20

Margutti R. et al., 2018, ApJ, 856, 18

Mesler R. A., Pihlström Y. M., Taylor G. B., Granot J., 2012, ApJ, 759, 4

Mooley K. P. et al., 2018, Nature, 554, 207

Mészáros P., Rees M. J., Wijers R. A. M. J., 1998, ApJ, 499, 301

Nakamura K., Shigeyama T., 2006, ApJ, 645, 431

Nakar E., Piran T., 2018, MNRAS, 478, 407

Nakar E. et al., 2018, preprint (arXiv:1803:07595)

Nicholl M. et al., 2017, ApJ, 848, L18

Panaitescu A., Kumar P., 2000, ApJ, 543, 66

Pian E. et al., 2017, Nature, 551, 67

Pihlström Y. M., Taylor G. B., Granot J., Doeleman S., 2007, ApJ, 664, 411

Ramirez-Ruiz E., Dray L. M., Madau P., Tout C. A., 2001, MNRAS, 327, 829

Ramirez-Ruiz E., García-Segura G., Salmonson J. D., Pérez-Rendón B., 2005, ApJ, 631, 435

Resmi L. et al., 2018, preprint (arXiv:1803.02768)

Rossi A. et al., 2018, GCN Circular #22763

Rossi E. M., Lazzati D., Rees M. J., 2002, MNRAS, 332, 945

Rossi E. M., Lazzati D., Salmonson J. D., Ghisellini G., 2004, MNRAS, 354, 86

Ruan J. J., Nynka M., Haggard D., Kalogera V., Evans P., 2018, ApJ, 853, L4

Salafia O. S., Ghisellini G., Ghirlanda G., 2018, MNRAS, 474, L7

Sari R., 1998, ApJ, 494, L49

Sari R., 1999, ApJ, 524, L43

Sari R., Mészáros P., 2000, ApJ, 535, L33

Sari R., Piran T., 1995, ApJ, 455, L143

Smartt S. J. et al., 2017, Nature, 551, 75

Soares-Santos M. et al., 2017, ApJ, 848, L16

Tanvir N. R. et al., 2017, ApJ, 848, L27

Taylor G. B., Frail D. A., Berger E., Kulkarni S. R., 2004, ApJ, 609, L1

Taylor G. B., Granot J., 2006, Mod. Phys. Lett. A, 21, 2171

Taylor G. B. et al., 2005, ApJ, 634, L93

Troja E. et al., 2017, Nature, 551, 71

Troja E. et al., 2018, MNRAS, 00, 00

Valenti S. et al., 2017, ApJ, 848, L24

van Marle A. J., Langer N., Achterberg A., García-Segura G., 2006, A&A, 460, 105

Villar V. A. et al., 2017, ApJ, 851, L21

Zhang B., Mészáros P., 2002, ApJ, 571, 876

## APPENDIX

### A1 Analytic scalings for a radial structure

Here, we consider a spherical outflow with a distribution of energy as a function of the ejecta's proper velocity, $E(> u) = E_0 u^{-s}$. For an external density $\rho = AR^{-k}$, the swept up mass within radius $R$ is $M(< R) = [4\pi/(3-k)]AR^{3-k}$. Beyond the deceleration radius $(R > R_d)$, assuming that the flow expands adiabatically, we have $E(> u) = E_0 u^{-s} = M(< R)c^2 u^2$ so that

$$u(R) = \left[\frac{(3-k)E_0}{4\pi Ac^2 R^{3-k}}\right]^{1/(2+s)} \propto R^{-(3-k)/(2+s)}. \quad (A1)$$

In the relativistic regime $u \approx \Gamma \gg 1$ and the observer time (for $z \approx 0$) $t \approx R/2c\Gamma^2$ so that

$$\Gamma(t) \approx \left[\frac{(3-k)E_0}{2^{5-k}\pi Ac^{5-k}t^{3-k}}\right]^{1/(8-2k+s)} \propto t^{-(3-k)/(8-2k+s)}, \quad (A2)$$

and $E_{k,iso} \propto \Gamma^{-s} \propto t^{(3-k)s/(8-2k+s)}$. Since $R \propto \Gamma^2 t \propto t^{(2+s)/(8-2k+s)}$ this implies that $F_\nu^{(G)} \propto \rho^{1/2} E_{k,iso}^{(3+p)/4} t^{(3-3p)/4} \propto t^\alpha$ with $\alpha = [(3-k)s(3+p) - 2k(2+s)]/[4(8-2k+s)] + (3-3p)/4$. An observed value of $\alpha$ could be reproduced by

$$s = \frac{2k + (8-2k)(4\alpha + 3p - 3)}{(3-k)(3+p) - 2k - 4\alpha - 3p + 3} \xrightarrow{k \to 0} \frac{8\alpha + 6p - 6}{3 - \alpha}, \quad (A3)$$

which for the parameters relevant for GRB 170817A $(k = 0, p = 2.2, \alpha = 0.8)$ implies $s \approx 6.2$.

In the Newtonian regime $u \approx \beta \ll 1$ and $R \sim \beta ct$ (for $z \approx 0$) so that $\beta \propto t^{-(3-k)/(5-k+s)}$ and $R \propto t^{(2+s)/(5-k+s)}$. The peak flux scales as $F_{\nu,max} \propto BN_e \propto \rho^{1/2}\beta R^{3-k} \propto R^{3-3k/2}\beta$ while the typical synchrotron frequency scales as $\nu_m \propto B\gamma_m^2 \propto \rho^{1/2}\beta^5 \propto R^{-k/2}\beta^5$ leading to $F_\nu^{(G)} \propto F_{\nu,max}\nu_m^{(p-1)/2} \propto t^\alpha$ with $\alpha = [(2+s)(12-5k-kp) - (6-2k)(5p-3)]/[4(5-k+s)]$ for which an observed value of $\alpha$ could be reproduced by (also see e.g. Nakar & Piran 2018)

$$s = \frac{2(15p - 21 + 10\alpha) - k[8(p-2) + 4\alpha]}{4(3-\alpha) - k(5+p)} \xrightarrow{k \to 0} \frac{15p - 21 + 10\alpha}{6 - 2\alpha}, \quad (A4)$$

which for the parameters relevant for GRB 170817A $(k = 0, p = 2.2, \alpha = 0.8)$ implies $s \approx 4.5$.

### A2 Analytic scalings for an angular structure

Here, we consider a relatively simple angular structure of a jet with a narrow uniform core at an angle $\theta_c \ll 1$ with power-law wings in $E_{k,iso} = 4\pi(dE/d\Omega)$ where $E_{k,iso}(\theta > \theta_c) \propto \theta^{-a}$, viewed at an angle $\theta_{obs}$ from its symmetry axis. For simplicity, we assume that the jet retains its initial angular structure (i.e. we neglect lateral spreading) and assume that at each angle $\theta$ from the jet's symmetry axis the flow evolves as if it were a part of a spherical flow with the local $E_{k,iso}(\theta)$. In this scenario the jet is relativistic and gradually decelerates as it sweeps up the external medium. At each observed time $t$ the parts of the jet that can significantly contribute to the observed emission are those whose beaming cone (of half-opening angle $1/\Gamma(\theta, t)$ around their direction of motion, which is assumed to be radial here) includes our line of sight. Therefore, they can be

treated as viewed 'on axis', and satisfy the usual on-axis relations

$$\Gamma = \sqrt{\frac{(3-k)E_{k,iso}(\theta)}{4\pi A c^2 R^{3-k}}} = \left[\frac{(3-k)E_{k,iso}(\theta)}{2^{5-k}\pi A c^{5-k} t^{3-k}}\right]^{1/(8-2k)}, \qquad (A5)$$

where $R \approx 2\Gamma^2 ct \propto [E_{k,iso}(\theta)t]^{1/(4-k)}$ and $\rho \propto R^{-k}$. Smaller $\theta$ corresponds to larger $E_{k,iso}$ and therefore higher $\Gamma$ for the same $t$. Therefore, at each $t$ there is a minimal angle $\theta = \theta_{min}(t)$ for which this condition

$$\theta_{obs} - \theta_{min}(t) = \frac{1}{\Gamma[\theta_{min}(t), t]} \qquad (A6)$$

is satisfied. For all $\theta > \theta_{min}(t)$ the beaming cone includes our line of sight, $\theta_{obs} - \theta < 1/\Gamma(\theta, t)$, i.e. their beaming cone includes our line of sight. Therefore, each such region of $\Delta\theta \sim \theta$ around $\theta$ would produce a flux corresponding to a spherical flow with the local $E_{k,iso}(\theta)$ times the fraction $f_\Omega \sim [\Gamma(\theta, t)\theta]^2$ of the solid angle $\sim\Gamma(\theta, t)^{-2}$ that would be observed for such a truly spherical flow that is actually occupied by such a region (of solid angle $\sim\theta^2$).

For PLS G, $F_\nu^{(G)} \propto f_\Omega \rho^{1/2} E_{k,iso}^{(3+p)/4} t^{(3-3p)/4}$. For a given $t$, $f_\Omega \sim [\Gamma(\theta, t)\theta]^2 \propto \theta^2 E_{k,iso}(\theta)^{1/2(4-k)} \propto \theta^{2-a/2(4-k)}$, $\rho^{1/2} \propto R^{-k/2} \propto E_{k,iso}(\theta)^{-k/2(4-k)} \propto \theta^{ak/2(4-k)}$ and $E_{k,iso}^{(3+p)/4} \propto \theta^{-a(3+p)/4}$ so that altogether $F_\nu^{(G)} \propto \theta^{2-a[(3+p)/4+(1-k)/2(4-k)]}$. For $k = 0$ and $p = 2.2$ the flux decreases with $\theta$ for $a > 1.4$, which holds for the values of $a$

that are relevant for this scenario. Therefore, the observed flux is dominated by the contribution from $\theta \sim \theta_{min}(t)$.

The emission becomes continuously dominated by more energetic regions of smaller $\theta_{min}(t)$ so that they quickly satisfy $\theta_{min} \ll \theta_{obs}$ and one can approximate $\theta_{obs} - \theta_{min} \approx \theta_{obs}$ in equation (A6), so that $\Gamma[\theta_{min}(t), t] \approx 1/\theta_{obs} = $ constant, and therefore equation (A5) implies that $E_{k,iso}[\theta_{min}(t)] \propto \theta_{min}(t)^{-a} \propto t^{3-k}$ and $\theta_{min}(t) \propto t^{-(3-k)/a}$, which in turn imply that $f_\Omega \sim (\theta_{min}/\theta_{obs})^2 \propto \theta_{min}^2 \propto t^{-2(3-k)/a}$. Given these scalings we obtain that $F_\nu^{(G)} \propto f_\Omega \rho^{1/2} E_{k,iso}^{(3+p)/4} t^{(3-3p)/4} \propto t^\alpha$ for $\alpha = (3-k)(a-2)/a - k(p+1)/4$, for which an observed values of $\alpha$ could be reproduced by

$$a = \frac{8(3-k)}{4(3-k) - 4\alpha - k(p+1)} \xrightarrow{k\to 0} \frac{6}{3-\alpha}. \qquad (A7)$$

For the parameters relevant for GRB 170817A ($k = 0$, $p = 2.2$, $\alpha = 0.8$), this implies $a \approx 2.7$, which in turn implies $\theta_{min}(t) \propto t^{-1.1}$, $f_\Omega \propto t^{-2.2}$, and $E_{k,iso} \propto t^3$ (and $E_{k,iso}^{(3+p)/4} \propto t^{3.9}$, $t^{(3-3p)/4} \to t^{-0.9}$) while the true energy in the region dominating the emission is $\sim\theta_{min}^2 E_{k,iso}(\theta_{min}) \propto \theta_{min}^{2-a} \propto t^{(3-k)(a-2)/a} \to t^{0.8}$ (for $k = 0$ it always scales as $t^\alpha$).